

Large diatom bloom off the Antarctic Peninsula during cool conditions associated with the 2015/2016 El Niño

Raul Rodrigo Costa ^{1,2}, Carlos Rafael Borges Mendes ^{1,2}, Afonso Ferreira^{1,3}, Virginia Maria Tavano^{1,2}, Tiago Segabinazzi Dotto^{2,5} & Eduardo Resende Secchi⁴

Diatoms play crucial functions in trophic structure and biogeochemical cycles. Due to poleward warming, there has been a substantial decrease in diatom biomass, especially in Antarctic regions that experience strong physical changes. Here we analyze the phytoplankton contents of water samples collected in the spring/summer of 2015/2016 off the North Antarctic Peninsula during the extreme El Niño event and compare them with corresponding satellite chlorophyll-*a* data. The results suggest a close link between large diatom blooms, upper ocean physical structures and sea ice cover, as a consequence of the El Niño effects. We observed massive concentrations (up to 40 mg m⁻³ of in situ chlorophyll-*a*) of diatoms coupled with substantially colder atmospheric and oceanic temperatures and high mean salinity values associated with a lower input of meltwater. We hypothesize that increased meltwater concentration due to continued atmospheric and oceanic warming trends will lead to diatom blooms becoming more episodic and spatially/temporally restricted.

¹Laboratório de Fitoplâncton e Microorganismos Marinhos, Instituto de Oceanografia, Universidade Federal do Rio Grande (FURG), Av. Itália, km 8, Rio Grande, RS 96203-900, Brazil. ²Laboratório de Estudos dos Oceanos e Clima, Instituto de Oceanografia, Universidade Federal do Rio Grande (FURG), Av. Itália, km 8, Rio Grande, RS 96203-900, Brazil. ³MARE—Centro de Ciências do Mar e do Ambiente, Faculdade de Ciências, Universidade de Lisboa, 1749-016 Campo Grande, Lisboa, Portugal. ⁴Laboratório de Ecologia e Conservação da Megafauna Marinha, Instituto de Oceanografia, Universidade Federal do Rio Grande (FURG), Av. Itália, km 8, Rio Grande, RS 96203-900, Brazil. ⁵Present address: Centre for Ocean and Atmospheric Sciences, School of Environmental Sciences, University of East Anglia, Norwich, UK. ✉email: raul_rodrigoc@hotmail.com

Poleward shifts in distribution and composition of species are a major evidence of climate warming consequences^{1–3}. Along the most warming-impacted regions of the Southern Ocean, with a myriad of cascading effects across all higher trophic levels, shifts from large to smaller phytoplankton cells have already been reported in marine ecosystems^{1,4,5}. With long-term global climate warming, the West Antarctic Peninsula (WAP) has been experiencing one of the largest atmospheric warming rates on Earth since the 1950s⁶. Together with atmospheric warming, there have been long-term increases in upper ocean temperatures⁷, marine glaciers retreating^{8,9}, and significant sea ice season reduction¹⁰. These long-term physical changes have led to substantial ecosystem alterations, namely in abundance and composition of phytoplankton groups across the WAP, although there have been marked meridional differences^{1,4,5}. Whereas the polar conditions are persisting along the mid/southern WAP, with a southward increase in phytoplankton biomass and diatom abundance over time^{1,3,11}, in the northern WAP region (hereafter Northern Antarctic Peninsula; NAP) these biological changes are particularly dramatic^{1,12}. With its key role at the base of the food web, a downward trend in phytoplankton biomass due to a decrease (increase) in abundance of large diatoms (small-sized cryptophytes) has been observed in situ along the NAP^{13,14}.

The NAP marine system, which encompasses the Gerlache and Bransfield Straits, the southernmost sector of the Drake Passage, and the northwestern Weddell Sea, is a diverse region featuring a range of oceanic and coastal ecosystems with complex hydrographic and biogeochemistry dynamics¹². The surface NAP waters can be split into cold and warm variety. The cold regime, located east of the Peninsula Front and southeast of the Elephant and Clarence islands, is sourced by transition waters from the Weddell Sea, which are generally characterized by low macronutrient concentrations¹⁵. In turn, the warm variety is mainly derived from the Antarctic Circumpolar Current surface waters, being distributed northwards along the NAP western continental shelves and the west of the Bransfield Front. The warm conditions west of the Peninsula Front are enriched of macronutrients in

subsurface waters as warm, nutrient- and carbon-rich Circumpolar Deep Water crosses the western Antarctic Peninsula continental shelves¹⁶. In addition, there is a northward surface water flow, from the Gerlache Strait to the warmer side of the Bransfield Strait, characterizing transition waters from the Bellingshausen Sea, which is responsible for advecting waters of a highly productive coastal zone to a more open region north of the NAP^{12,17,18}.

The trends of atmospheric warming and sea ice declining along the NAP, which have intensified in the mid-twentieth century, have slowed down since the late 1990s^{19,20}. This apparent recent short-term plateau of longer-term trends has been associated with regional wind pattern changes coupled with large-scale climate variability, such as Southern Annular Mode (SAM) and El Niño–Southern Oscillation¹⁶. During negative SAM/El Niño conditions, colder and weaker southerly winds blow across the region, resulting in high sea ice concentrations that reduce wind-mixing in winter and supply meltwater to upper ocean stabilization in spring/summer, enhancing phytoplankton-growth^{3,10,21}. The opposite occurs during positive SAM/La Niña. Additionally, the effects of positive SAM may be offset by El Niño conditions, leading to colder winds and increased sea ice extent along the NAP¹⁶.

The 2015/2016 El Niño was one of the strongest on record, with sea surface temperature anomalies exceeding 2.5 °C in the tropical Pacific Ocean²². Its effects were associated with high variability in sea ice extent along the Southern Ocean²³, and an unprecedented increase in the ice sheet accumulation over the Antarctic Peninsula²². Moreover, in the same period, an intense bloom of large centric diatoms was registered during the NAP summer²⁴, contrasting its long-term trend towards smaller phytoplankton cells^{1,12}. However, a clear relationship between the results of the intense diatom bloom and the effects of the extreme 2015/2016 El Niño event was not established. Here, we investigate the link between this first extreme El Niño of the twenty-first century²⁵ and the atypical seasonal phytoplankton succession dominated by diatoms, with massive concentrations, during the spring/summer of 2015/2016 along the NAP, using collected in situ data and remote sensing measurements. This provides a rare opportunity to understand how diatom succession dynamics can positively respond to the effects of an extreme El Niño event, a counterpoint to drivers of long-term warming trend in a changing NAP.

Results and discussion

Due to contrasts in oceanographic properties along the NAP²⁴, the sampling grid was split in two subregions: north and south (Fig. 1; see “Methods”). The north and south subregions showed from the satellite data a much higher spring/summer (November–February) mean chlorophyll-*a* (Chl-*a*) in 2015/2016 than the decadal average time series (2010–2019; Table 1). In agreement with the El Niño effects^{10,16}, the sea surface temperature (SST) and the air temperature showed substantially lower mean values during the spring/summer of 2015/2016 along the subregions (Table 1). However, there was an evident spatial/temporal variability in sea ice concentration/duration between the subregions, with a northward (southward) lower (higher) mean value during 2015/2016 in relation to the decadal average (Table 1). Along the south subregion during the spring/summer of 2015/2016, the increased Chl-*a* during January followed the decline in the sea ice concentration over the spring and early summer, concurrent with increased SST, which was markedly colder throughout the seasonal phytoplankton succession (Fig. 2a). These results to the south subregion are consistent with previous studies along the WAP, in which years characterized by

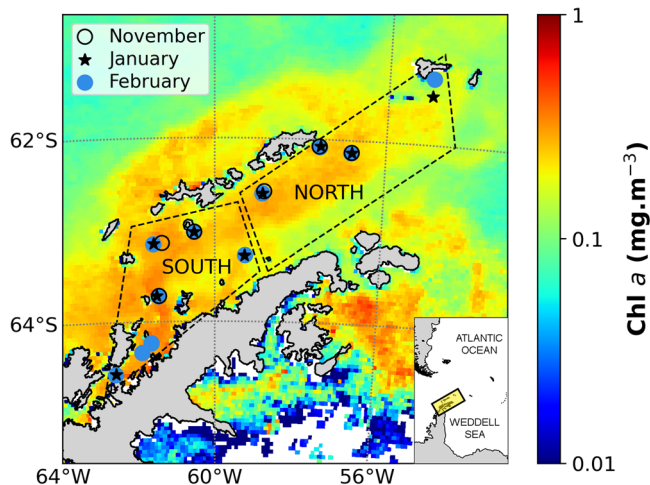


Fig. 1 Study area. Location of hydrographic stations is marked by open circles (November), stars (January), and blue circles (February). The black dashed lines indicate the subregions (north and south) along the NAP and delimit the areas used to estimate average remote sensing measurements. The decadal-mean (2010–2019) remote sensing chlorophyll-*a* (Chl-*a*) is exhibited in the background, indicating the biomass (Chl-*a*) distribution of phytoplankton along the NAP in the last decade. An inset map in the lower right corner shows the location of the NAP within the Atlantic sector of the Southern Ocean.

Table 1 Biological production and ocean/atmosphere parameters by measurements of remote sensing and local meteorological stations during spring/summer in the NAP subregions.

Variables	South			North		
	2010–2019	2015/2016	Diff	2010–2019	2015/2016	Diff
Chl- <i>a</i> (mg m^{-3})	0.23	0.57	0.34**	0.19	0.47	0.28**
SST ($^{\circ}\text{C}$)	0.50	0.14	-0.36**	0.21	-0.12	-0.33**
Air temperature ($^{\circ}\text{C}$)	0.81	0.17	-0.64**	0.03	-0.33	-0.36*
Sea ice concentration (%)	0.47	1.48	1.01**	0.87	0.29	-0.58**
Sea ice duration (days)	101	126	25	135	130	-5

Average of chlorophyll-*a* (Chl-*a*), sea surface temperature (SST), air temperature, and sea ice concentration during spring/summer (November–February) on a decadal average time series (2010–2019) and on 2015/2016 along the NAP subregions. The sea ice duration was also estimated to the decadal-mean and 2015/2016 (see “Methods”). Diff is the spring/summer difference value between the 2015/2016 and the decadal-mean. The positive (negative) values indicate that parameters were higher (lower) in the 2015/2016 spring/summer compared with the decadal average time series. Significant increase or decrease (-) of the parameters is indicated by asterisks, with a confidence limit of 95% (*) and 99% (**), using Student’s *t* test comparisons. The sea ice duration was not tested (see “Methods”).

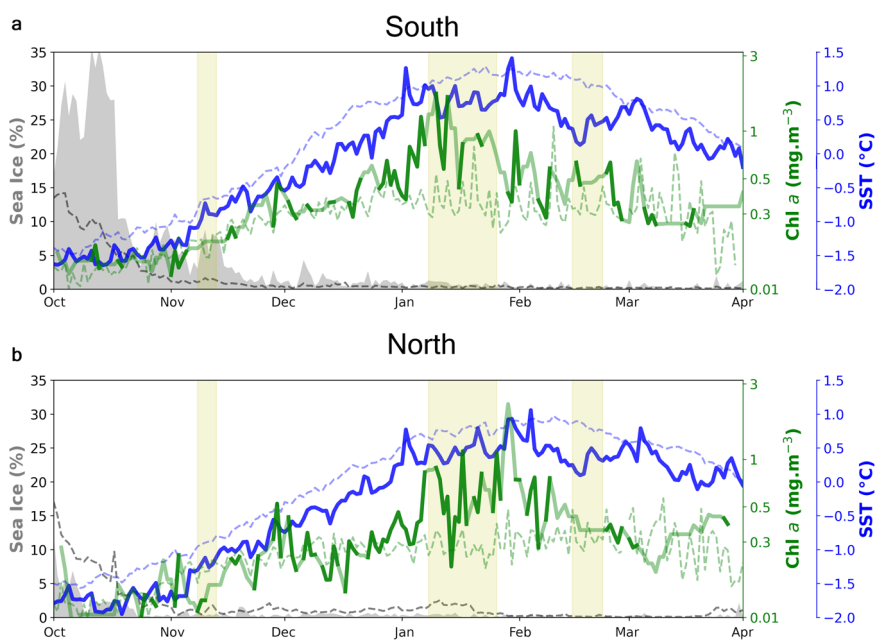


Fig. 2 Biological production and sea ice dynamics in the NAP seasonal phytoplankton succession of 2015/2016. Continuum remote sensing measurements of chlorophyll-*a* (Chl-*a*; solid green line), sea surface temperature (SST; solid blue line), and sea ice concentration (gray area) along the NAP, in south (a) and north (b) subregions during spring/summer of 2015/2016. The dashed green, blue and gray lines indicate the decadal average (2010–2019) of Chl-*a*, SST, and sea ice concentration, respectively. The solid light green lines represent the Chl-*a* interpolated values. The background shades show the in situ data sampling periods. It is important to note that Chl-*a* remote sensing data in Antarctic coastal waters are typically underestimated in respect to in situ Chl-*a* data (see Supplementary Fig. 1)^{12,29}.

longer sea ice cover in winter have led to higher phytoplankton biomass in the following summer associated with a more stable water column^{11,16,26}. To the north subregion, however, although there was a similar pattern between Chl-*a* and SST, the increased Chl-*a* during January was not related with the sea ice retreat (Fig. 2b). Moreover, there was a clear difference between the Chl-*a* peaks (the highest Chl-*a* value reached) along the subregions from the satellite data. The Chl-*a* peak in the south subregion occurred in early January (10 January 2016, reaching 1.73 mg m^{-3}), whereas in the north subregion the Chl-*a* peak was observed in late January (29 January 2016, reaching 2.23 mg m^{-3}).

It has been estimated that drifters entrained in the Gerlache Strait Current and the Bransfield Strait Current exit the Bransfield Strait in 10–20 days¹⁷, which is consistent with the interval of 19 days between both Chl-*a* peaks when considering the extreme distance between the subregions (see Fig. 1). These authors also estimated that drifters deployed in the Gerlache Strait Current were quickly advected out of the Gerlache Strait in less than

1 week (i.e., low residence time)¹⁷, which supports the similar diatom species assemblages identified in our microscopic analysis between stations of the Gerlache Strait and southwestern Bransfield Strait²⁴. Therefore, it is plausible that phytoplankton growth in the north of the Gerlache Strait may be laterally advected northward into the Bransfield Strait, explaining the observed concomitant increase of satellite Chl-*a* data in both subregions from spring, associated with sea ice retreat southward (Fig. 2). In addition, as phytoplankton biomass tends to accumulate northward^{17,27,28}, the advection processes could also explain the temporal and intensity differences of the Chl-*a* peaks along the subregions (see Fig. 2). This suggests that there was a link between the sea ice dynamics, phytoplankton biomass (Chl-*a*) and advection processes along the NAP during the spring/summer of 2015/2016, in which the sea ice melting first triggered an increase in phytoplankton biomass through water column stratification along the south subregion, and the advection processes led to a subsequent increase northward.

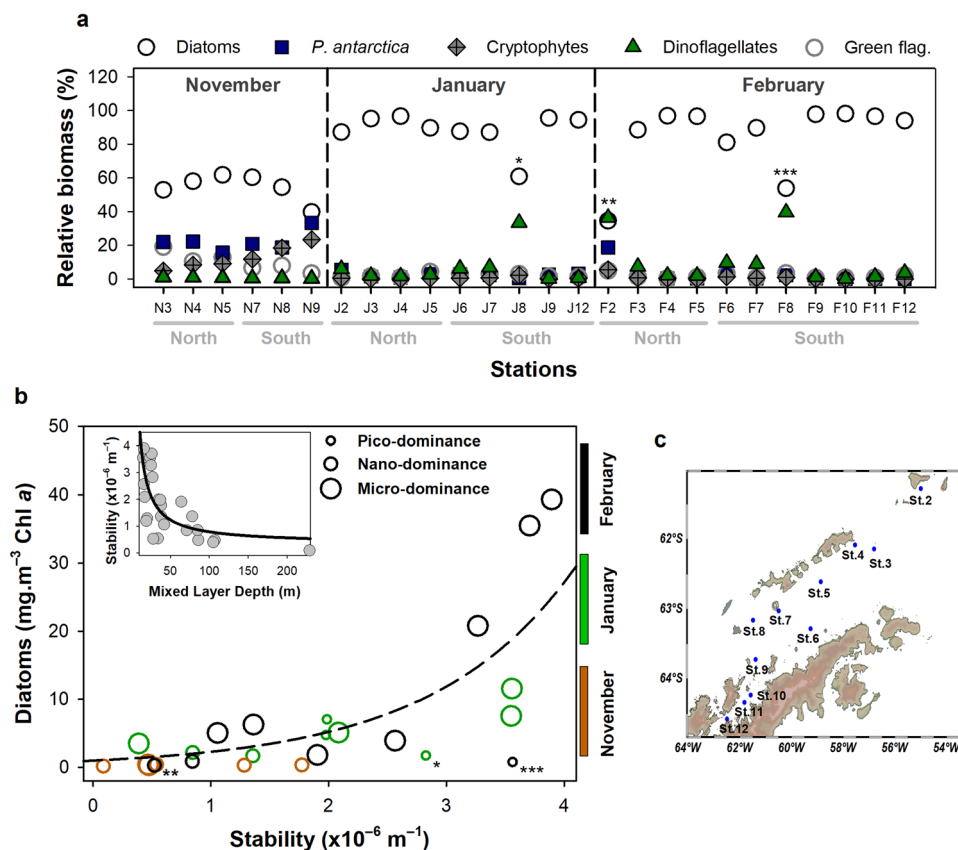


Fig. 3 Phytoplankton community composition and upper ocean physical structures along the NAP seasonal phytoplankton succession of 2015/2016.

a Relative biomass (to the total in situ chlorophyll-*a*; Chl-*a*) distribution of phytoplankton groups on surface, via HPLC/CHEMTAX analysis, during spring/summer of 2015/2016 along the NAP subregions. The black open circles indicate diatoms, the blue squares indicate *Phaeocystis antarctica*, the gray diamonds with crosses indicate cryptophytes, the green triangles indicate dinoflagellates, and the light gray open circles indicate green flagellates.

b Exponential curve ($R^2 = 0.57$; $p < 0.0001$; $n = 25$) between upper ocean stability (Stability) and diatom absolute concentrations on surface. Symbol size indicates phytoplankton size class (pico-, nano- or micro-phytoplankton) that dominated with values $>40\%$ the community composition proportion in respect to the total Chl-*a* (considering the three fractionated size classes). Symbol color indicates the sampling month in respect to November (brown), January (gray), and February (black). The inset shows the polynomial inverse relationship ($R^2 = 0.51$; $p < 0.001$; $n = 26$) between mixed layer depth (MLD) and Stability and indicates that a shallow MLD is not necessarily stable. The subregions are indicated by the underscore gray line below the stations' number (**a**). The letter N, J, or F (November, January, and February, respectively) denotes the respective month of data sampling according to locations of fixed number stations represented by the map on the lower right corner (**c**). In (**a**, **b**), asterisks indicate decreased diatom proportion associated with increased dinoflagellate proportion during distinct moments of summer months (January and February).

The satellite Chl-*a* data require extensive validation with in situ data, especially in polar regions, where cloud cover is ubiquitous and performance is typically poor, due to not properly accurate Chl-*a* algorithms^{12,29}. For that, although the mean Chl-*a* in 2015/2016 from the satellite data was approximately twice as large as the decadal average, there was a severe discrepancy in the mean Chl-*a* values observed between the in situ and remote sensing data (see Table 1 and Supplementary Table 1). This highlights the importance of the in situ dataset reported here, especially evident during February 2016, when the signal of an intense diatom bloom ($> 40 \text{ mg m}^{-3}$ Chl-*a*)²⁴ was not captured in the satellite data (Supplementary Fig. 1), supporting that phytoplankton biomass accumulation during this summer was much higher than recorded by remote sensing observations (see Table 1). In general, the in situ Chl-*a* achieved its maximum (40 mg m^{-3}) and higher mean value (17.4 mg m^{-3}) during February comparing to November and January (Supplementary Table 1).

Phytoplankton community structure during the spring/summer of 2015/2016 was assessed through Chemical taxonomy (CHEMTAX) software, using accessory pigments versus in situ Chl-*a* concentrations measured via high-performance liquid chromatography (HPLC; see “Methods”). The main phytoplankton group over the

season were diatoms, followed by haptophytes (*Phaeocystis antarctica*), cryptophytes, and dinoflagellates, according to the succession stage (Fig. 3a). Diatoms dominated the phytoplankton community composition in relation to the other groups along the whole in situ sampling period, although their relative biomass (to the total in situ Chl-*a*) was lower in some stations compared to others in different moments during spring/summer (Fig. 3a). To assess the degree to which the water column structure was a primary driver for development and intensity of diatom growth^{3,24}, the mixed layer depth (MLD) and water column stability were calculated as a function of seawater potential density (see “Methods”). There was an inverse polynomial relationship between MLD and mean upper ocean stability (averaged over 5–150 m depth; hereafter referred to as upper ocean stability) (Fig. 3b). The significant positive exponential relationship between the upper ocean stability and diatom absolute concentrations (in situ Chl-*a*) demonstrates that stability, associated with MLD, was an important driver of diatom dynamics (Fig. 3b). This elucidates the increase in biological production during summer months of 2016, when upper ocean physical structures (MLD and stability) were sufficiently shallow and stable to produce the high phytoplankton biomass (in situ Chl-*a*) registered here. However, as MLD and stability showed similar values between summer months

(Supplementary Table 1), only the upper ocean physical structures cannot be accounted for the high differences of in situ Chl-*a* values observed between diatom blooms in January (maximum of 12 mg m⁻³) and February (maximum of 40 mg m⁻³). Likewise, also not explaining these differences of in situ Chl-*a* values between summer months, macronutrients were highly abundant throughout the seasonal phytoplankton succession (Supplementary Table 1). Furthermore, although no measurements of dissolved iron, which can be considered as a limiting factor to primary productivity³⁰, were carried out here, the Antarctic Peninsula continental shelves have been depicted as a substantial source of this micronutrient to the upper ocean, not limiting phytoplankton growth even during intense blooms^{31,32}.

The stability was also seen to influence the dominant phytoplankton size class. While micro-phytoplankton dominated over the whole range of the upper ocean stability, smaller size classes showed a more restricted distribution (Fig. 3b). These differences on biomass and dominant phytoplankton size class could be due to distinct moments of the succession stages linked to interspecific differences. In general, the nano- and pico-phytoplankton were more abundant when: (i) stability was lower in the late spring/early summer (mainly small diatoms and small flagellates) (Fig. 3b and Supplementary Fig. 2), and when (ii) the large micro-phytoplankton cells left the system in a fast-sinking process, leading to a shift to small dinoflagellates (mainly Gymnodiniales < 20 µm) in the late summer (Fig. 3b)²⁴.

To further examine these phytoplankton composition and biomass differences along the seasonal succession, the physiological condition and grazing pressure were also assessed through indices, using accessory pigments and Chl-*a* degradation products via HPLC analysis (see “Methods”). Predominantly, the highest proportions of photosynthetic carotenoids were observed in the mid/late summer, indicating high photosynthetic activity from the phytoplankton cells associated with diatom blooms. During the late spring, however, phytoplankton communities accumulated more photoprotective carotenoid pigments (see Supplementary Fig. 3a, b), likely to mitigate the cells photo-oxidative damage caused by enhanced irradiation, which favors species adapted to light stress³³. This indicates that the large environmental fluctuations characteristic of the spring, due to the physiological stress, typically favor a more heterogeneous community dominated by nanoflagellates and other smaller phytoplankton cells (Supplementary Fig. 2 and Fig. 3a, b)^{26,34}. The grazing and senescence indices, in turn, indicate that top-down control and phytoplankton cell deterioration, respectively, were more intense during January, compared to February, which may explain part of the monthly in situ Chl-*a* differences (Supplementary Fig. 3c, d).

The top-down control performing on phytoplankton biomass may be exerted by both microheterotrophs (e.g., bacteria, heterotrophic flagellates, and ciliates) and metazoan plankton, such as krill and salps. The fecal pellets of metazoans tend to sink quickly, and hence are improbable to be sampled³⁵. However, it is unlikely that in situ Chl-*a* could have reached the high values recorded here in January and February 2016 under a grazing pressure of metazoans^{30,36}. Therefore, it is expected that a grazing pressure associated with microheterotrophs was the major top-down control in this situation. Microheterotrophs differ from metazoans in that they are included together with phytoplankton during sample filtration for HPLC/CHEMTAX analysis and, consequently, pigments associated with their grazing, ingested and/or digested, are extracted and analyzed³⁵. Moreover, their small fecal pellets sink slowly and are thus likely to be captured with the sample³⁵. To support this case, converging with our grazing index data (Supplementary Fig. 3c), diatom blooms generally characterized by large centric cells were clearly different

between both summer periods. While in February the diatom bloom was mainly composed by the large centric *Odontella weissflogii* (mostly > 70 µm in length; ref. ²⁴), during January a large number (> 2.5 × 10⁶ cells L⁻¹) of small (< 20 µm in length) pennate *Fragilariopsis* spp. contributed substantially to the total of diatom bloom biomass. Given that large cell size of phytoplankton can reduce, or prevent, efficiency of zooplankton grazing^{37,38}, this intra-group difference between the diatom blooms may be indicating that a selective activity of micro-heterotrophic grazing occurred on smaller pennate diatoms during January 2016.

Furthermore, the effects of a strong positive SAM trend on sea ice dynamics over the previous years may have caused a severe impact on the survival of larval krill², which was reflected in low krill recruit density during 2016 along the NAP³⁹. This further supports a low top-down control from the krill population during this summer, which is also consistent with the grazing index values that were much lower than expected (Supplementary Fig. 3c, d)²⁴. It has been recorded along the Antarctic regions that these grazing index values are greater than 10% when associated with diatom blooms^{40,41}, thus indicating a prevalence of active grazing pressure. Therefore, it is likely that the low top-down control on produced biomass further contributed to the high anomalous values of in situ Chl-*a* registered over the seasons; even though a grazing pressure associated with micro-heterotrophic zooplankton assemblages may have driven differences in Chl-*a* concentrations between the mid/late summer (Supplementary Fig. 3c, d).

Despite the clear dominance of diatoms throughout the in situ sampling periods in the 2015/2016 spring/summer, there was a notable separation between November and January/February in respect to the biomass contribution (as a proportion to the total Chl-*a*) of the main phytoplankton functional groups (Supplementary Fig. 4). Using a canonical correspondence analysis (see “Methods”), the diatoms and dinoflagellates were positively associated with temperature, stability and Chl-*a*, and negatively associated with salinity, MLD and macronutrients to the mid/late summer months. The opposite was observed with the other phytoplankton groups (mostly small nanoflagellates), mainly associated with the stations sampled during November (Supplementary Fig. 4), as discussed above. This indicates that, during summer months, dinoflagellates (mainly Gymnodiniales < 20 µm) were the second most representative taxonomic group, after diatoms.

To determine the statistical relationship between diatoms and dinoflagellates along the NAP seasonal succession, all in situ data collected during February 2016 (ref. ²⁴), along with the dataset presented here, were further assessed. In general, there was a positive relationship between absolute concentrations of both groups, suggesting their coexistence (Supplementary Fig. 5a). It is possible to observe that there was a decline in diatom biomass under higher values of upper ocean stability, mainly associated with waters influenced by ice melt coming from the Bellingshausen Sea (Supplementary Fig. 5a)²⁴. This was linked to the sedimentation process of larger diatom cells out of the upper layers, due to water column structure dynamics²⁴. As a result, following the diatom sinking process, the significant positive relationship between upper ocean stability and dinoflagellates further indicates that these small flagellates were a major contributor for the phytoplankton community composition in the late summer 2016 (Supplementary Figs. 5b and 6). In recent years, it has been observed an increasingly contribution of small dinoflagellates (especially Gymnodiniales < 20 µm) to phytoplankton community composition along the NAP waters during the mid/late summer months^{42–44}, drawing attention to potential poleward shifts of Antarctic phytoplankton species¹². These small

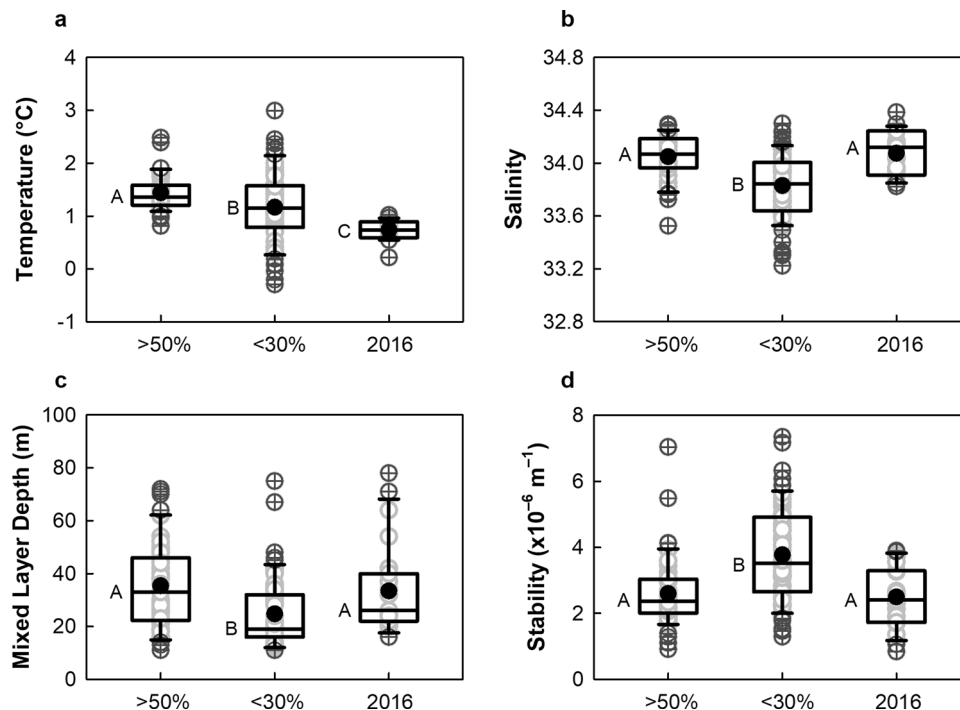


Fig. 4 Differences on water physical parameters between diatom proportions in the NAP late summer. a–d Box plots of surface temperature (**a**), surface salinity (**b**), mixed layer depth (MLD; **c**), and upper ocean stability (**d**) for >50% (time series: 2008–2015, 2017), <30% (time series: 2008–2015, 2017), and 2016 (>50%) regarding to diatom proportion to the total chlorophyll-*a* (Chl-*a*; see “Methods”). The horizontal lines of the boxes indicate the median and the 25th and 75th percentiles. The dark gray circles with crosses indicate the outliers, and the light gray open circles indicate the individual values. Average values are presented by black closed circles. The whiskers extend to values not considered as outliers. Kruskal–Wallis tests were applied to determine the difference among groups (see “Methods”) (**a**: $H_2 = 39.0$, $p < 0.001$; **b**: $H_2 = 29.3$, $p < 0.001$; **c**: $H_2 = 16.2$, $p < 0.001$; **d**: $H_2 = 28.3$, $p < 0.001$). The capital letters indicate statistical groupings, which statistically differ each other at $p < 0.05$, based on all pairwise multiple comparison procedures with Dunn’s Method. In (**a–d**), $n = 48$, 68, and 23 for >50%, <30%, and 2016, respectively.

flagellates have been reported apparently occupying sites/conditions less favorable to diatoms and cryptophytes^{24,42}. Furthermore, going into autumn (from March onwards), the decline in SST may still suggest a period of increased wind speed, and thus vertical mixing, which indicates a potential deepening of MLD along the region. This event, together with progressive reduced daylight length⁴⁵, could further explain the decline in Chl-*a* values from the satellite data to the end of the seasonal phytoplankton succession (Fig. 2), potentially favouring a community dominated by small mixed flagellates and small diatoms (Supplementary Fig. 6)⁴⁵.

Kruskal–Wallis tests were performed (see “Methods”), comparing our February time series data (2008–2017) with the atypical situation of February 2016 (our focus here), to examine differences on water physical parameters and on indices of physiological state and grazing pressure associated with high (> 50%) and low (< 30%) diatom proportions (to the total in situ Chl-*a*). In general, high diatom proportion (representing values in the time series and in 2016 higher than 50%) showed a strong association with deeper MLD (> 20 m), higher surface salinity (majority > 34), and lower upper ocean stability values ($< 4 \times 10^{-6} \text{ m}^{-1}$) relative to low diatom proportion (representing values in the time series lower than 30%; see Fig. 4). These results demonstrate a preferential fundamental niche to diatoms along the NAP (Fig. 4), although there was a marked difference in biomass accumulation during February 2016 (see Supplementary Fig. 7). In addition, there were also strong differences on indices of physiological state and grazing pressure between high and low diatom proportions. The low proportion of diatoms was associated with higher (lower) ratios of photoprotective (photosynthetic) carotenoids and lower (higher) grazing (senescence)

index values, which suggest a poorly productive phytoplankton community relative to high diatom proportion conditions (Supplementary Fig. 8).

The only physical parameter showing a difference between both high diatom proportions was surface temperature, which was colder in 2016. However, this parameter solely cannot explain the much higher diatom biomass observed in the late summer 2016 (mean Chl-*a* value of 12.4 mg m^{-3}) relative to the other years (mean Chl-*a* values lower than 1 mg m^{-3} ; see Supplementary Fig. 7). The ratios of photoprotective carotenoids and senescence index showed higher values in the other years (2008–2015, 2017) compared with 2016, pointing for a less favorable condition during these years, even though no statistically significant difference between the ratios of photosynthetic carotenoids and grazing index was found (see Supplementary Fig. 8). As high diatom proportions showed similar behavior regarding water physical parameters (Fig. 4), differences on both photoprotective and senescence indices may be indicating that less favorable conditions^{35,40–42} were preventing diatom biomass accumulation in the other years compared with 2016. However, only through the indices is not possible to disentangle the potential critical factor associated with these unfavorable conditions. Analyses of diatom life cycle, considering interspecific differences, prevailing irradiance, and nutrient availability (mainly those in trace amounts) will be needed to evaluate, and understand, the critical factor (factors) which is (are) hampering diatom bloom formation, even under favorable upper ocean physical structures. The difference in space and time should be considered, assuming the likelihood of sedimentation process (or consumption by metazoan plankton) of large diatom cells before the sampling, that is, low diatom biomass but favorable upper

ocean physical structures. Furthermore, although there was no statistical difference between grazing index values associated with high diatom proportions; activity of grazing in the other years cannot be disregarded as a potential driver on diatom biomass, as the grazing index in these years in respect to 2016 showed a wide range of values, which in part exceeded 10% (see Supplementary Fig. 8c).

Over a longer spatial/temporal scale, the effects of climate warming are progressing southward beyond the NAP^{1,3}. The progression of these effects is causing impacts on ocean physics and biological compartments. Accordingly, a decrease in diatom proportion has been pointed northward along the mid/southern WAP, concurrent with an increase in cryptophyte proportion³. This shift has also been reported along the NAP as a result of glacier meltwater processes during summer^{12–14}. Due to meltwater inputs, the cryptophyte fundamental niche has been associated along the NAP with mean values of salinity lower than 34 (refs. ^{13,14}), which is consistent with other regions in the mid/southern WAP^{3,11,46}. Moreover, it has also been observed that the peak of cryptophyte abundance is related to warmer air temperature (> 2.3 °C), contrasting with diatom peak that was found at lower mean air temperature (~ 1.2 °C)¹¹. Such evidence links the reported trends of an increase in cryptophyte proportion and warmer ocean and atmospheric temperatures, which play a pivotal role in glacier retreat rates, driving a substantial glacial melting over the past warming decades along the Antarctic Peninsula^{8,9,16}.

During the spring/summer of 2015/2016 reported here, diatom blooms were associated with lower mean air temperatures and high mean surface salinity values (< 0.2 °C and > 34 , respectively; see Fig. 4, Table 1, and Supplementary Table 1), which could be indicating a lower incoming of meltwater¹⁶. Likewise, during the moderately strong 2009/2010 El Niño event, large diatom blooms along the NAP coastal region were associated with low air temperature, which caused a delay in the melting of surrounding glaciers, leading to average salinity values greater than 34 (ref. ⁴⁷). These findings are consistent with our results, which reinforce that the effects of the extreme 2015/2016 El Niño on atmospheric/ocean physics were substantial, triggering anomalous diatom blooms during the seasonal phytoplankton succession (Fig. 4). However, even with large diatom blooms during recent El Niño events, the cryptophyte growth has still been reported along the NAP^{13,45}. The emergence of this nanoflagellate was associated with localized inputs of glacial meltwater, decoupled from the diatom blooms, supporting the segregation and/or competition between these two phytoplankton functional groups^{11,12}. This differentiation in upper ocean physical structures caused by the influence of glacial meltwater input, which leads to shallower, stabilized, and well-lit upper layers, based on results found here, apparently prevents diatom bloom formation along the NAP due to the fast-sinking process, decreasing biomass accumulation (Fig. 4d and Supplementary Fig. 5a). It is important to note that, in a first moment, diatom contribution increased concomitantly with the upper ocean stability (Fig. 3), decreasing its biomass on contrary under higher stability values ($> 4 \times 10^{-6} \text{ m}^{-1}$; Supplementary Fig. 5a). These results converge with the distribution of low diatom proportion associated with higher (lower) upper ocean stability (surface salinity) and shallower MLD (Fig. 4b–d). Additionally, other factors such as daily, seasonal and latitudinal fluctuations in solar radiation^{41,48}, top-down control^{30,49}, inter-specific differences³³, and micronutrient limitations¹⁶ within the upper ocean cannot be disregarded for further understanding diatom dynamics along the NAP, and in other Antarctic coastal regions.

The substantial long-term physical changes along the NAP have been linked to strengthening winds, driven by a positive

SAM trend and its co-variability with La Niña^{1,10,16}. However, this is opposed to the results reported here, in which the effects of the extreme 2015/2016 El Niño notably superimposed on the persistent positive SAM trend. In this study, we demonstrated a close link between large diatom blooms, upper ocean physical structures and sea ice cover during the spring/summer of 2015/2016 along the NAP (Figs. 2–4). Moreover, there was also evidence of low top-down control on the diatom biomass (Supplementary Figs. 3c and 8c), which further supports that bottom-up control is a key mechanism of the marine ecosystems along the WAP⁵⁰. As it is predicted by models that positive SAM frequencies will increase for the next 50 years⁵¹, coupled with strong winds and warmer temperatures, further glacial retreat and sea ice decline⁶ should be expected. Consequently, this would provide a more favorable fundamental niche for cryptophytes^{3,12}. This hypothetical future scenario would make large diatom blooms typically episodic events, intensifying and/or establishing what it has been observed over the past warming decades across the NAP^{1,12–14,47}. Therefore, despite a seasonal phytoplankton succession with massive concentrations of diatoms during the austral spring/summer of 2015/2016; due to continued warming trends, diatom blooms may become more episodic and restricted at spatial/temporal scales with increasingly meltwater inputs along the NAP.

Methods

Cruise design and sampling collection. Data for this study were collected during three seasonal oceanographic cruises conducted on board the *RV Almirante Maximiano* of the Brazilian Navy during the late spring and mid/late summer months (November, January and February, respectively) between 2015 and 2016 along the NAP. The study area covered the northern sector of the Gerlache Strait, which separates the Anvers and Brabant Islands from the Antarctic Peninsula, and the Bransfield Strait, located between the Southern Shetland Islands and the Peninsula (Fig. 1). The NAP is a diverse region featuring a range of oceanic and coastal ecosystems with complex hydrographic and biogeochemistry dynamics, which are strongly influenced by transition waters from the Weddell and Bellingshausen Seas¹². Therefore, the NAP sampling grid in this study was split in two subregions: north and south (Fig. 1). The sampling grid consists of nine fixed numbering stations (Fig. 3), which overall were systematically sampled during the three seasonal oceanographic cruises. However, during November due to persistent extended sea ice cover some fixed stations were not sampled (Fig. 1). On the other hand, during February two additional stations (Sts. 10 and 11) were performed to better evaluate the massive diatom bloom observed (Figs. 1 and 3)²⁴. In addition, the *Brazilian High Latitude Oceanography Group* (GOAL) time series data (2008–2017) were also used here. These data were compiled over 10 years of oceanographic cruises conducted on board the polar vessels *Ary Rongel* (2008–2010) and *Almirante Maximiano* (2013–2017) of the Brazilian Navy during the austral late summer (February) from 2008 to 2017 along the NAP. There were no cruises performed in the years of 2011 and 2012. From 2008 to 2010 there were no measurements in the Gerlache Strait, only in the Bransfield Strait.

A combined Sea-Bird CTD (conductivity–temperature–depth instrument)/Carrousel 911+system[®] equipped with 24 five-litre Niskin bottles was used to measure the hydrographic data profiles, such as in situ temperature (°C) and salinity. Seawater discrete samples were collected at regular depths of 5, 25, 50, 75, 100, and 150 m using Niskin bottles to characterize the vertical distribution of phytoplankton communities. Surface seawater samples (5 m) were taken in all CTD stations for both dissolved nutrients and phytoplankton pigments analyses. These seawater samples (0.5–2.5 L) were filtered under low vacuum through GF/F filters, which were subsequently frozen in liquid nitrogen for later HPLC/CHEMTAX analysis. Additionally, size fractionation of phytoplankton biomass (mg m^{-3} Chl-*a*) was performed through sequential filtering of surface water samples (1000 mL). Each surface sample for size fractionation was firstly filtered using a polycarbonate filter with pore size of 20 μm (GE Water & Process Technologies, 47 mm). The collected filtrate was subsequently filtered into a polycarbonate filter with pore size of 2 μm (GE Water & Process Technologies, 47 mm). Ultimately, the collected filtrate was filtered into GF/F filter (Whatman) to retain the cells between 0.7 and 2 μm . The first two filtrations were performed by gravity and the last under low vacuum pump (< 5 in. Hg). The filtration by gravity minimizes risks of breaking phytoplankton cells. The filters of size fractionation were also frozen in liquid nitrogen for later HPLC/CHEMTAX analysis. This procedure yielded measurements of concentrations of Chl-*a* (mg m^{-3}) and other pigments, as well as phytoplankton functional groups' contributions for the pico-phytoplankton (0.7–2 μm), nano-phytoplankton (2–20 μm), and micro-phytoplankton (> 20 μm).

Physical measurements. Seawater thermodynamic calculations were performed with the Thermodynamic Equation of Seawater—2010 (TEOS-10)⁵³. For each CTD cast, the seawater potential density (ρ , kg m⁻³) referenced to 0 dbar was determined based on seawater conservative temperature, absolute salinity and pressure data. To examine the water column physical structure, MLD (m) and water column stability ($\times 10^{-6}$ m⁻¹) were calculated from 5-m smoothed profiles of ρ , due to the high surface variability. Although recent studies have estimated MLD through the depth of the maximum water column buoyancy frequency (N^2), this method does not consider the strength of stratification, but only the homogeneity of the upper ocean layer^{3,21}. Therefore, to determine the variation of MLD apart of the strength of stratification, MLD was calculated as the depth at which ρ deviates from its 10 m depth value by a threshold of $\Delta\rho = 0.03$ kg m⁻³ (ref. 54). The water column stability was estimated through the N^2 by the local gravity, using vertical ρ variations²⁴.

To represent the variation of stability values estimated to each meter within the upper ocean layers, the mean stability between 5 and 150 m (upper ocean stability) was used based on the analysis of ref. 24. It is important to note that despite of MLD and upper ocean stability are not completely independent, since both are calculated from the ρ , their statistical relationship is not linear; that is, a shallow MLD is not necessarily stable (Fig. 3b).

Dissolved nutrients analysis. Cellulose acetate membrane filters were used to filtrate the surface seawater samples to determine dissolved inorganic nutrients (i.e., dissolved inorganic nitrogen—DIN: nitrate, nitrite and ammonium; phosphate and silicic acid). Samples were immediately frozen at -80°C until the laboratory analysis. Nutrients were analyzed following the spectrophotometric determination methods described in ref. 55 at the Laboratory of Biogeochemistry at the Federal University of Rio de Janeiro, Brazil. In the form of reactive Si, silicic acid measurements were corrected for sea salt interference. Reaction with ammonium molybdate was used to measure orthophosphate, with absorption readings at 885 nm.

HPLC/CHEMTAX analysis. In the laboratory, the filters were placed in a screw-cap centrifuge tube with 3 mL of 95% cold-buffered methanol (2% ammonium acetate) containing 0.05 mg L⁻¹ trans- β -apo-8'-carotenal (Fluka) as internal standard. Samples were sonicated for 5 min in an ice-water bath and placed at -20°C for 1 h. Then, samples were centrifuged at $1100 \times g$ for 5 min at 3°C . To separate the extract from remains of filter and cell debris, the supernatants were filtered through Fluoropore PTFE membrane filters (0.2 μm pore size). Immediately prior to injection, 1000 μL of sample was mixed with 400 μL of Milli-Q water in 2.0 mL amber glass sample vials, which then were placed in the HPLC cooling rack (4°C). A Shimadzu HPLC constituted by a solvent distributor module (LC-20AD) with a control system (CBM-20A), a photodiode detector (SPDM20A), and a fluorescence detector (RF-10AXL) was used to analyze the pigment extracts. The chromatographic separation of the pigments was performed using a monomeric C8 column (SunFire; 15 cm long; 4.6 mm in diameter; 3.5 μm particle size) at a constant temperature of 25°C . The mobile phase (solvent) and respective gradient followed the method developed by ref. 56, which was discussed and optimized⁵⁷, with a flow rate of 1 mL min⁻¹, injection volume of 100 μL , and 40 min runs. The absorbance spectra and retention times were used to identify the pigments. The concentrations of the pigments were calculated from the signals in the photodiode array detector in comparison with commercial standards obtained from DHI (Institute for Water and Environment, Denmark). LC-Solution software was used to integrate the peaks that were checked manually and corrected when necessary. In order to correct for losses and volume changes, the concentrations of the pigments were normalized to the internal standard. To reduce the uncertainty of pigments found in low concentrations⁵⁸, a quality assurance threshold procedure through application of quantification limit (LOQ) and detection limit (LOD) was applied to the pigment data. The LOQ and LOD procedures were performed according to ref. 57.

Three types of Chl-*a* degradation products: chlorophyllide-*a* (Chlide-*a*), pheophytin-*a* (Phytin-*a*), and pheophorbide-*a* (Phide-*a*) were identified and quantified by HPLC analysis. The sum of the Phytin-*a* and Phide-*a* was used to calculate the proxy of grazing pressure, while Chlide-*a* was used to calculate the senescence of phytoplankton cells^{40,41,59}. These two indices were divided by the total of degradation products plus Chl-*a* (sum of Chl-*a*, Phytin-*a*, Phide-*a* and Chlide-*a*), and represented as a percentage (Supplementary Fig. 3c, d).

The phytoplankton community faces variable light regimes within only one single day, when mixed up to the surface from depth, experiencing high irradiance on top, which contrasts with low irradiance at the base of MLD⁴⁸. To efficiently maximize ambient light regimes the phytoplankton cells adjust their photosynthetic apparatus, expanding their light-harvesting complexes under low light conditions, or synthesizing photoprotective pigments under high light conditions, which prevent photodamage⁶⁰. Therefore, via HPLC analysis, photopigment indices were used to investigate phytoplankton pigment acclimations in response to different environmental regimes^{40,42}. The carotenoids were separated into photosynthetic carotenoids (PSCs) and photoprotective carotenoids (PPCs). The PSC included 19'-butanoyloxyfucoxanthin, 19'-hexanoyloxyfucoxanthin, fucoxanthin, prasinoxanthin and peridinin, whereas the PPC were composed by zeaxanthin, violaxanthin, lutein, alloxanthin, diadinoxanthin, diatoxanthin, β , β -carotene and β , ϵ -carotene⁶¹. Thus, two photo-pigment indices were derived and used here, PSC: Chl-*a* and PPC: Chl-*a*. These indices show the proportion of each

carotenoid pigment group (PSCs and PPCs) to the total biomass (Chl-*a*). It is important to highlight that phytoplankton pigment composition may be influenced by photoacclimation processes and nutrient availabilities^{48,60,62}. Despite phytoplankton responses could take time scales of hours to days, our analyses associated with PSC: Chl-*a* and PPC: Chl-*a* include a wide scale of space and time with our time series of 2008–2017 sampled during February months (Supplementary Fig. 8). Therefore, it is possible to access the state (taking into account the large number of samples in space and time, which allow us obtaining reference values) by which phytoplankton communities were being exposed and subsequently acclimated, thus indicating in part the environmental conditions associated with these cells, under stress or not. The difference in taxonomic composition should also be considered.

The class-specific accessory pigments and total Chl-*a* were used to calculate the absolute and relative contribution of phytoplankton groups through the Chemical taxonomy (CHEMTAX) software v1.95 (ref. 63). CHEMTAX uses a factor analysis and steepest descent algorithm to best fit the data onto an initial matrix of pigment ratios (the ratios between the respective accessory pigments and Chl-*a*). This software package has been extensively and successfully used in many worldwide investigations, including in the Southern Ocean^{3,13,14,24}, to determine the distribution and biomass of phytoplankton functional groups. This approach provides valuable information about the whole phytoplankton community, including small-size species, which are normally difficult to identify by light microscopy. The Chl-*a* was used in this study as a proxy for biomass^{64,65}, once this photosynthetic pigment is common to all autotrophic phytoplankton. Therefore, we use the term Chl-*a* referring to either absolute biomass or relative biomass attributed to the corresponding taxonomic groups.

Seven algal groups were chosen for CHEMTAX analysis based on initial pigment ratios derived for the NAP (ref. 42). The groups resolved include diatoms Type-A, diatoms Type-B, dinoflagellates Type-A, dinoflagellates Type-B, cryptophytes, haptophytes type 8 (*Phaeocystis antarctica*) and green flagellates. The two types of diatoms (diatoms Type-A and diatoms Type-B) were grouped as a same chemotaxonomic group: the diatoms. The two types of dinoflagellates (dinoflagellates Type-A and dinoflagellates Type-B) were also grouped as a same chemotaxonomic group: the dinoflagellates. It is important to note that diatoms Type-A were not considered in the analysis of CHEMTAX during February 2016, due to the absence of chlorophyll *c*₁ (ref. 24). Similarly, during November 2015, the diatoms Type-A and dinoflagellates Type-B were not considered in the analysis of CHEMTAX, due to the absence of chlorophyll *c*₁ and gyroxanthin esters, respectively.

The pigment dataset was separated in two distinct subregions: north and south (Fig. 1). These subregion datasets were further split into three bins according to sample depth (0–25 m, 25–50 m and > 50 m), each of which was separately analyzed by CHEMTAX to allow for variation in pigment: Chl-*a* ratios with depth⁶⁶. Regarding the fractionation data, an additional split of both pigment datasets was performed according to size class (> 20 μm , 2–20 μm , 0.7–2 μm). This procedure assures a homogeneity of the pigment: Chl-*a* ratios, considering all samples from the same bin, and provides some compensation for changes in these ratios, which are known to vary with light availability^{67,68}. Series of 60 pigment ratio matrices were generated for optimization of the input matrix by multiplying each ratio from the initial matrix by a random function as described in ref. 69. The average of the best six (10%) output matrices (with the lowest residual or mean square root error) was taken as the optimized result to each bin. Lastly, the results of phytoplankton chemotaxonomic groups derived from the CHEMTAX were quality-controlled by microscopic analysis.

Remote sensing analysis. Daily L3 Chl-*a* (mg m⁻³) data with spatial resolution of 4×4 km were acquired from the ESA Ocean Colour Climate Change Initiative (OC-CCI)⁷⁰ product (v4) for the period 1997–2019. This product merges satellite ocean color data from four separate ocean color sensors: the Sea-Viewing Wide Field-of-View Sensor (SeaWiFS; 1997–2010), the Medium Resolution Imaging Spectrometer (MERIS; 2002–2012), the Moderate Resolution Imaging Spectroradiometer (MODIS; 2002–present) and the Visible Infrared Imaging Radiometer Suite (VIIRS; 2011–present). In order to integrate measurements from each sensor, data are band-shifted to match the SeaWiFS bands and subsequently bias-corrected. The OC-CCI product is validated with extensive in-situ datasets, exhibiting high correlation at a global level ($R^2 = 0.73$)⁷¹.

2010–2019 Satellite SST ($^\circ\text{C}$) and sea ice concentration (%) were extracted from the ESA SST CCI and C3S global Sea Surface Temperature Reprocessed product (available at CMEMS)⁷². This product provides gap-free daily-averaged data with a spatial resolution of 5×5 km at a global level. SST data were merged from measurements obtained from the Along Track Scanning Radiometer (ATSR), Sea and Land Surface Temperature Radiometer (SLSTR) and the Advanced Very High Resolution Radiometer (AVHRR) sensors. Sea ice concentration data were obtained from the EUMETSAT Ocean and Sea Ice Satellite Application Facility (OSI-SAF) OSI-450 and OSI-430. Sea ice duration (days) was defined based on the analysis of ref. 10: as an interval between the sea ice advance in autumn and sea ice retreat in spring. Day of advance is identified when sea ice concentration first exceeds 15% (i.e., the approximate ice edge) for at least 5 days, whereas the day of retreat is identified when sea ice concentration remains below 15% until the end of the study period.

For all measured variables (except sea ice duration), including air temperature (recorded at local meteorological stations), daily means were calculated for all pixels inside each subregion (north and south; Fig. 1) from the early November to the end of February (defined as spring/summer here) for a period of 10 years (2010–2019). The November–February mean was determined to the austral spring/summer of 2015/2016 and to the 10 years of the time series, which includes every austral spring/summer into this period, characterizing the decadal average (Figs. 1, 2 and Table 1). The estimated sea ice duration, as a difference between the advance and retreat of sea ice from the satellite data, was calculated to each year over the 10 years. Then, sea ice duration for the decadal average represents an average considering all years, whereas the sea ice duration for 2015/2016 was estimated as a sole value between advance (April) and retreat (September) of sea ice of 2015, which reflected during the spring/summer of 2015/2016. These averages were used to assess the intensity of the effects associated with the extreme 2015/2016 El Niño^{22,25}, with respect to the decadal pattern of the analyzed variables along the NAP, which were mainly influenced by the persistent positive SAM trend^{2,16}.

Air temperature. Daily surface air temperature (°C) measured at the Antarctic bases of Palmer Station (64°46′27″S 64°03′10″W; south region) and Base Presidente Eduardo Frei Montalva (62°12′0″S 58°57′51″W; north region) were acquired from the Global Historical Climatology Network (GHCN; available via NOAA Climate Data Online—<https://www.ncdc.noaa.gov/cdo-web/>) for the period between 2010 and 2019.

Statistical analysis. Relationships between biomass (in situ Chl-*a*) of phytoplankton groups and environmental variables at surface (except stability, which was defined as the mean upper ocean stability between 5 and 150 m, and MLD) were determined through canonical correspondence analysis (CCA) using CANOCO for Windows 4.5 software⁷³. Biotic variables were represented by the CHEMTAX-derived taxonomic groups' relative biomass (as a proportion to the total Chl-*a*). Environmental variables included upper ocean stability (Stability), MLD, sea surface temperature (Temperature), sea surface salinity (Salinity), dissolved inorganic nitrogen (DIN), phosphate (Phosphate) and silicic acid (Silicic acid). All variables were log-transformed before analysis to reduce the influence of different scales in the datasets. In order to evaluate the significance of the CCA, Monte-Carlo tests were run based on 499 permutations under a reduced model ($p = 0.002$).

For north and south subregions, differences in the spring/summer average values from the satellite data of Chl-*a*, SST, air temperature, and sea ice concentration between the decadal-mean and 2015/2016 were analyzed using Student's *t* test comparisons (Table 1). This statistical analysis was not performed for sea ice duration because this parameter is presented as a sole value, which prevents the use of Student's *t* test comparisons. Kruskal–Wallis tests were performed, comparing our February time series data (2008–2017) with the atypical situation of February 2016 (our focus here) to examine differences on water physical parameters, physiological state (indices) and grazing index values associated with high (> 50%) and low (< 30%) diatom proportions. This is a nonparametric test. February data (from 2008 to 2015 and 2017) were split in two bins regarding diatom proportion to the total biomass (in situ Chl-*a*): > 50% and < 30%. Then, these two bins, along with diatom proportion higher than 50% in February 2016, were statistically tested to access potential differences of diatom distribution in respect to environmental settings (Fig. 4 and Supplementary Fig. 8).

Data availability

The phytoplankton chemotaxonomic dataset and associated indices used here are fully available at <https://doi.org/10.5281/zenodo.5592163>. The hydrographic dataset is available at ref.⁵². The chlorophyll-*a* from remote sensing measurements can be accessed at https://www.oceancolour.org/thredds/catalog-cci.html?dataset=CCL_ALL-v4.2-DAILY. The sea surface temperature and sea ice concentration from remote sensing measurements can be accessed at https://resources.marine.copernicus.eu/product-detail/SST_GLO_SST_L4_REP_OBSERVATIONS_010_011/INFORMATION. The air temperature measurements are available at <https://www.ncdc.noaa.gov/data/global-historical-climatology-network-daily/>.

Received: 16 November 2020; Accepted: 19 November 2021;

Published online: 09 December 2021

References

- Montes-Hugo, M. et al. Recent changes in phytoplankton communities associated with rapid regional climate change along the western Antarctic Peninsula. *Science* **323**, 1470–1473 (2009).
- Atkinson, A. et al. Krill (*Euphausia superba*) distribution contracts southward during rapid regional warming. *Nat. Clim. Change* **9**, 142–147 (2019).
- Brown, M. S. et al. Enhanced oceanic CO₂ uptake along the rapidly changing West Antarctic Peninsula. *Nat. Clim. Change* **9**, 678–683 (2019).
- Schofield, O. et al. How do polar marine ecosystems respond to rapid climate change? *Science* **328**, 1520–1523 (2010).
- Ducklow, H. W. et al. West Antarctic Peninsula: an ice-dependent coastal marine ecosystem in transition. *Oceanography* **26**, 190–203 (2013).
- Turner, J. et al. Antarctic climate change and the environment: an update. *Polar Rec.* **50**, 237–259 (2014).
- Meredith, M. P. & King, J. C. Rapid climate change in the ocean west of the Antarctic Peninsula during the second half of the 20th century. *Geophys. Res. Lett.* **32**, L19604 (2005).
- Cook, A. J., Fox, A. J., Vaughan, D. G. & Ferrigno, J. G. Retreating glacier fronts on the Antarctic Peninsula over the past half-century. *Science* **308**, 541–544 (2005).
- Cook, A. J. et al. Ocean forcing of glacier retreat in the western Antarctic Peninsula. *Science* **353**, 283–286 (2016).
- Stammerjohn, S. E., Martinson, D. G., Smith, R. C., Yuan, X. & Rind, D. Trends in Antarctic annual sea ice retreat and advance and their relation to El Niño–Southern oscillation and Southern Annular Mode variability. *J. Geophys. Res. Oceans* **113**, C03S90 (2008).
- Schofield, O. et al. Decadal variability in coastal phytoplankton community composition in a changing West Antarctic Peninsula. *Deep-Sea Res. Part I Oceanogr. Res. Pap.* **124**, 42–54 (2017).
- Ferreira, A. et al. Changes in phytoplankton communities along the northern Antarctic Peninsula: causes, impacts and research priorities. *Front. Mar. Sci.* **7**, 576254 (2020).
- Mendes, C. R. B. et al. Shifts in the dominance between diatoms and cryptophytes during three late summers in the Bransfield Strait (Antarctic Peninsula). *Polar Biol.* **36**, 537–547 (2013).
- Mendes, C. R. B. et al. New insights on the dominance of cryptophytes in Antarctic coastal waters: a case study in Gerlache Strait. *Deep-Sea Res. Part II Top. Stud. Oceanogr.* **149**, 161–170 (2018).
- Kang, S. H., Kang, J. S., Lee, S., Chung, K. H., Kim, D. & Park, M. G. Antarctic phytoplankton assemblages in the marginal ice zone of the northwestern Weddell Sea. *J. Plankton Res.* **23**, 333–352 (2001).
- Henley, S. F. et al. Variability and change in the west Antarctic Peninsula marine system: research priorities and opportunities. *Prog. Oceanogr.* **173**, 208–237 (2019).
- Zhou, M., Niiler, P. P. & Hu, J. Surface currents in the Bransfield and Gerlache Straits, Antarctica. *Deep-Sea Res. Part I Oceanogr. Res. Pap.* **49**, 267–280 (2002).
- Savidge, D. K. & Amft, J. A. Circulation on the West Antarctic Peninsula derived from 6 years of shipboard ADCP transects. *Deep-Sea Res. Part I Oceanogr. Res. Pap.* **59**, 1633–1655 (2009).
- Oliva, M. et al. Recent regional climate cooling on the Antarctic Peninsula and associated impacts on the cryosphere. *Sci. Total Environ.* **580**, 210–223 (2017).
- Turner, J. et al. Absence of 21st century warming on Antarctic Peninsula consistent with natural variability. *Nature* **535**, 411–415 (2016).
- Schofield, O. et al. Changes in the upper ocean mixed layer and phytoplankton productivity along the West Antarctic Peninsula. *Phil. Trans. R. Soc. Lond. A* **376**, 20170173 (2018).
- Bodart, J. A. & Bingham, R. J. The impact of the extreme 2015–2016 El Niño on the mass balance of the Antarctic ice sheet. *Geophys. Res. Lett.* **46**, 13862–13871 (2019).
- Stuecker, M. F., Bitz, C. M. & Armour, K. C. Conditions leading to the unprecedented low Antarctic sea ice extent during the 2016 austral spring season. *Geophys. Res. Lett.* **44**, 9008–9019 (2017).
- Costa, R. R. et al. Dynamics of an intense diatom bloom in the Northern Antarctic Peninsula, February 2016. *Limnol. Oceanogr.* **65**, 2056–2075 (2020).
- Santoso, A., McPhaden, M. J. & Cai, W. The defining characteristics of ENSO extremes and the strong 2015/2016 El Niño. *Rev. Geophys.* **55**, 1079–1129 (2017).
- Rozema, P. D. et al. Interannual variability in phytoplankton biomass and species composition in northern Marguerite Bay (West Antarctic Peninsula) is governed by both winter sea ice cover and summer stratification. *Limnol. Oceanogr.* **62**, 235–252 (2017).
- Smith, D. A., Hofmann, E. E., Klinck, J. M. & Lascara, C. M. Hydrography and circulation of the West Antarctic Peninsula Continental Shelf. *Deep-Sea Res. Part I Oceanogr. Res. Pap.* **46**, 925–949 (1999).
- García, M. A. et al. Water masses and distribution of physico-chemical properties in the Western Bransfield Strait and Gerlache Strait during Austral summer 1995/96. *Deep-Sea Res. Part II Top. Stud. Oceanogr.* **49**, 585–602 (2002).
- Dietersen, H. M. & Smith, R. C. Bio-optical properties and remote sensing ocean color algorithms for Antarctic Peninsula waters. *J. Geophys. Res. Oceans* **105**, 26301–26312 (2000).
- Assmy, P. et al. Thick-shelled, grazer-protected diatoms decouple ocean carbon and silicon cycles in the iron-limited Antarctic Circumpolar Current. *Proc. Natl Acad. Sci. USA* **110**, 20633–20638 (2013).
- Bown, J. et al. Bioactive trace metal timeseries during Austral summer in Ryder Bay, Western Antarctic Peninsula. *Deep-Sea Res. Part II Top. Stud. Oceanogr.* **139**, 103–119 (2017).

32. Sherrell, R. M. et al. A ‘shallow bathtub ring’ of local sedimentary iron input maintains the Palmer deep biological hotspot on the West Antarctic Peninsula shelf. *Phil. Trans. R. Soc. Lond. A* **376**, 20170171 (2018).
33. Petrou, K. et al. Southern Ocean phytoplankton physiology in a changing climate. *J. Plant Physiol.* **203**, 135–150 (2016).
34. Joy-Warren, H. et al. Light is the primary driver of early season phytoplankton production along the Western Antarctic Peninsula. *J. Geophys. Res. Oceans* **124**, 7375–7399 (2019).
35. Wright, S. W. et al. Phytoplankton community structure and stocks in the Southern Ocean (30–80°E) determined by CHEMTAX analysis of HPLC pigment signatures. *Deep-Sea Res. Part II Top. Stud. Oceanogr.* **57**, 758–778 (2010).
36. Holm-Hansen, O. & Mitchell, B. G. Spatial and temporal distribution of phytoplankton and primary production in the western Bransfield Strait region. *Deep-Sea Res. Part A* **38**, 961–980 (1991).
37. Quetin, L. B. & Ross, R. M. in *Feeding by Antarctic Krill, Euphausia superba: Does Size Matter? Antarctic Nutrient Cycles and Food Webs* (eds. Siegfried, W. R. et al.) 372–377 (Springer, Berlin, 1985).
38. Opaliński, K. W., Maciejewska, K. & Georgieva, L. V. Notes of food selection in the Antarctic krill, *Euphausia superba*. *Polar Biol.* **17**, 350–357 (1997).
39. Walsh, J., Reiss, C. S. & Watters, G. M. Flexibility in Antarctic krill *Euphausia superba* decouples diet and recruitment from overwinter sea-ice conditions in the northern Antarctic Peninsula. *Mar. Ecol. Prog. Ser.* **642**, 1–19 (2020).
40. Mendes, C. R. B. et al. Dynamics of phytoplankton communities during late summer around the tip of the Antarctic Peninsula. *Deep-Sea Res. Part I Oceanogr. Res. Pap.* **65**, 1–14 (2012).
41. Pillai, H. U. K. et al. Planktonic food web structure at SSTF and PF in the Indian sector of the Southern Ocean during austral summer 2011. *Polar Res.* **37**, 1495545 (2018).
42. Mendes, C. R. B. et al. Impact of sea ice on the structure of phytoplankton communities in the northern Antarctic Peninsula. *Deep-Sea Res. Part II Top. Stud. Oceanogr.* **149**, 111–123 (2018).
43. Mascioni, M. et al. Phytoplankton composition and bloom formation in unexplored nearshore waters of the western Antarctic Peninsula. *Polar Biol.* **42**, 1859–1872 (2019).
44. Mascioni, M. et al. Microplanktonic diatom assemblages dominated the primary production but not the biomass in an Antarctic fjord. *J. Marine Syst.* **224**, 103624 (2021).
45. Pan, B. J. et al. Environmental drivers of phytoplankton taxonomic composition in an Antarctic fjord. *Prog. Oceanogr.* **183**, 102295 (2020).
46. Moline, M. A., Claustre, H., Frazer, T. K., Schofield, O. & Vernet, M. Alteration of the food web along the Antarctic Peninsula in response to a regional warming trend. *Glob. Change Biol.* **10**, 1973–1980 (2004).
47. Schloss, I. R. et al. On the phytoplankton bloom in coastal waters of southern King George Island (Antarctica) in January 2010: an exceptional feature? *Limnol. Oceanogr.* **59**, 195–210 (2014).
48. Alderkamp, A., de Baar, H. J. W., Visser, R. J. W. & Arrigo, K. R. Can photoinhibition control phytoplankton abundance in deeply mixed water columns of the Southern Ocean? *Limnol. Oceanogr.* **55**, 1248–1264 (2010).
49. Garibotti, I. A., Vernet, M., Kozłowski, A. & Ferrario, M. E. Composition and biomass of phytoplankton assemblages in coastal Antarctic water: a comparison of chemotaxonomic and microscopic analyses. *Mar. Ecol. Prog. Ser.* **247**, 27–42 (2003).
50. Saba, G. K. et al. Winter and spring controls on the summer food web of the coastal West Antarctic Peninsula. *Nat. Commun.* **5**, 4318 (2014).
51. Gillett, N. P. & Fyfe, J. C. Annular mode change in the CMIP5 simulations. *Geophys. Res. Lett.* **40**, 1189–1193 (2013).
52. Dotto, T. S., Mata, M. M., Kerr, R. & Garcia, C. A. E. A novel hydrographic gridded data set for the northern Antarctic Peninsula. *Earth Syst. Sci. Data* **13**, 671–696 (2021).
53. McDougall, T. J. & Barker, P. M. Getting started with TEOS-10 and the Gibbs Seawater (GSW) Oceanographic Toolbox (SCOR/IAPSO WG127, 2011).
54. de Boyer Montégut, C., Madec, G., Fischer, A. S., Lazar, A. & Iudicone, D. Mixed layer depth over the global ocean: an examination of profile data and a profile based climatology. *J. Geophys. Res.* **109**, C12003 (2004).
55. Aminot, A. & Chaussepied, M. Manuel des analyses chimiques en milieu marin. Centre National pour l’Exploitation des Océans (CNEXO, Brest, 1983).
56. Zapata, M., Rodríguez, F. & Garrido, J. L. Separation of chlorophylls and carotenoids from marine phytoplankton: a new HPLC method using a reversed phase C8 column and pyridine-containing mobile phases. *Mar. Ecol. Prog. Ser.* **195**, 29–45 (2000).
57. Mendes, C. R., Cartaxana, P. & Brotas, V. HPLC determination of phytoplankton and microphytobenthos pigments: comparing resolution and sensitivity of a C18 and a C8 method. *Limnol. Oceanogr. Methods* **5**, 363–370 (2007).
58. Hooker, S. B. et al. *The Second Sea-WiFS HPLC Analysis Round-Robin Experiment (SeaHARRE-2)* (NASA Goddard Space Flight Center, Maryland, 2005).
59. Jeffrey, S. W. Profiles of photosynthetic pigments in the ocean using thin-layer chromatography. *Mar. Biol.* **26**, 101–110 (1974).
60. Van Leeuwe, M. A., Van Sikkelerus, B., Gieskes, W. W. C. & Stefels, J. Taxon-specific differences in photoacclimation to fluctuating irradiance in an Antarctic diatom and a green flagellate. *Mar. Ecol. Prog. Ser.* **288**, 9–19 (2005).
61. Araujo, M. L. V., Mendes, C. R. B., Tavano, V. M., Garcia, C. A. E. & Baringer, M. O. N. Contrasting patterns of phytoplankton pigments and chemotaxonomic groups along 30°S in the subtropical South Atlantic Ocean. *Deep-Sea Res. Part I Oceanogr. Res. Pap.* **120**, 112–121 (2017).
62. Van De Poll, W. H., Van Leeuwe, M. A., Roggeveld, J. & Buma, A. G. J. Nutrient limitation and high irradiance acclimation reduce PAR and UV-induced viability loss in the Antarctic diatom *Chaetoceros brevis* (Bacillariophyceae). *J. Phycol.* **41**, 840–850 (2005).
63. Mackey, M. D., Mackey, D. J., Higgins, H. W. & Wright, S. W. CHEMTAX—a program for estimating class abundances from chemical markers: application to HPLC measurements of phytoplankton. *Mar. Ecol. Prog. Ser.* **144**, 265–283 (1996).
64. Jeffrey, S. W., Mantoura, R. F. C. & Wright, S. W. *Phytoplankton Pigments in Oceanography: Guidelines to Modern Methods* (UNESCO, Paris, 1997).
65. Huot, Y. et al. Relationship between photosynthetic parameters and different proxies of phytoplankton biomass in the subtropical ocean. *Biogeosciences* **4**, 853–868 (2007).
66. Mackey, D. J., Higgins, H. W., Mackey, M. D. & Holdsworth, D. Algal class abundances in the western equatorial Pacific: estimation from HPLC measurements of chloroplast pigments using CHEMTAX. *Deep-Sea Res. Part I Oceanogr. Res. Pap.* **45**, 1441–1468 (1998).
67. Schlüter, L., Møhlenberg, F., Havskum, H. & Larsen, S. The use of phytoplankton pigments for identifying and quantifying phytoplankton groups in coastal areas: testing the influence of light and nutrients on pigment/chlorophyll a ratios. *Mar. Ecol. Prog. Ser.* **192**, 49–63 (2000).
68. Higgins, H. W., Wright, S. W. & Schlüter, L. in *Quantitative interpretation of chemotaxonomic pigment data. Phytoplankton Pigments: Characterization, Chemotaxonomy and Applications in Oceanography* (eds. Roy, S. et al.) 257–313 (Cambridge University Press, United Kingdom, 2011).
69. Wright, S. W., Ishikawa, A., Marchant, H. J., Davidson, A. T., van den Enden, R. L. & Nash, G. V. Composition and significance of picophytoplankton in Antarctic waters. *Polar Biol.* **32**, 797–808 (2009).
70. Sathyendranath, S. et al. An ocean-colour time series for use in climate studies: the experience of the ocean-colour climate change initiative (OC-CCI). *Sensors* **19**, 4285 (2019).
71. Jackson, T. et al. *Ocean Colour Climate Change Initiative—Product User Guide* (European Space Agency, 2019).
72. Merchant, C. J. et al. Satellite-based time-series of sea-surface temperature since 1981 for climate applications. *Sci. Data* **6**, 223 (2019).
73. Ter Braak, C. J. F. & Prentice, I. C. A theory of gradient analysis. *Adv. Ecol. Res.* **18**, 271–317 (1988).

Acknowledgements

This is a multidisciplinary study as part of the Brazilian High Latitude Oceanography Group (GOAL) activities in the Brazilian Antarctic Program (PROANTAR). This study has received funding from the European Union’s Horizon 2020 research and innovation program under grant agreement no. 810139: Project Portugal Twinning for Innovation and Excellence in Marine Science and Earth Observation—PORTWIMS. Financial support was also provided by National Council for Research and Development (CNPq) and Coordination for the Improvement of Higher Education Personnel (CAPES). This study was conducted within the activities of the INTERBIOTA, NAUTILUS, PRO-VOCCAR, ECOPELAGOS (CNPq grant numbers 407889/2013-2, 405869/2013-4, 442628/2018-8, 442637/2018-7, respectively) and CMAR2 (CAPES grant number 23038.001421/2014-30) projects. The authors thank the crew of the *RV Almirante Maximiano* of the Brazilian Navy and several scientists and technicians participating in the cruise for their valuable help during sampling. We are grateful to Simon Wright, from the Australian Antarctic Division, for providing the CHEMTAX v.1.95 software; Ricardo Pollery, from Federal University of Rio de Janeiro, for performing the nutrient analysis; Pedro Félix, from Federal University of Rio Grande, by carrying out part of the HPLC/CHEMTAX analysis; and to Márcio de Souza, from Federal University of Rio Grande, for performing the microscopic analysis. T.S.D. acknowledge financial support from the CNPq-Brazil PDJ scholarship (151248/2019-2). A.F. received a Ph.D. grant from Fundação para a Ciência e a Tecnologia (FCT; grant no. SFRH/BD/144586/2019). Additional support from the FCT was also given to this study (UID/MAR/04292/2020). R.R.C., C.R.B.M. and E.R.S. are granted with research fellowships from CNPq. CAPES also provided free access to many relevant journals through the portal “Periódicos CAPES”. This study is within the scope of two Projects of the Institutional Internationalization Program (Capes Print-FURG –Edital 41/2017). This research is also framed within the College on Polar and Extreme Environments (Polar2E) of the University of Lisbon. We are thankful for the constructive criticism of the three anonymous reviewers, who helped to improve the manuscript.

Author contributions

R.R.C. and C.R.B.M. carried out the HPLC/CHEMTAX analyses. A.F. and T.S.D. performed the remote sensing and the physical oceanography analyses, respectively. R.R.C. and C.R.B.M. contributed to the conception and design of this work and wrote the first draft of the manuscript. R.R.C. and A.F. designed the figures. A.F., V.M.T., T.S.D., and E.S. contributed to the organization and writing of the final version of the manuscript. All authors contributed to manuscript revision, read, and approved the submitted version.

Competing interests

The authors declare no competing interests.

Additional information

Supplementary information The online version contains supplementary material available at <https://doi.org/10.1038/s43247-021-00322-4>.

Correspondence and requests for materials should be addressed to Raul Rodrigo Costa.

Peer review information *Communications Earth & Environment* thanks Jose Luis Iriarte Machuca and the other, anonymous, reviewer(s) for their contribution to the peer review of this work. Primary handling editors: Sze Ling Ho, Joe Aslin. Peer reviewer reports are available.

Reprints and permission information is available at <http://www.nature.com/reprints>

Publisher's note Springer Nature remains neutral with regard to jurisdictional claims in published maps and institutional affiliations.



Open Access This article is licensed under a Creative Commons Attribution 4.0 International License, which permits use, sharing, adaptation, distribution and reproduction in any medium or format, as long as you give appropriate credit to the original author(s) and the source, provide a link to the Creative Commons license, and indicate if changes were made. The images or other third party material in this article are included in the article's Creative Commons license, unless indicated otherwise in a credit line to the material. If material is not included in the article's Creative Commons license and your intended use is not permitted by statutory regulation or exceeds the permitted use, you will need to obtain permission directly from the copyright holder. To view a copy of this license, visit <http://creativecommons.org/licenses/by/4.0/>.

© The Author(s) 2021